RSC Advances

ROYAL SOCIETY OF CHEMISTRY

www.rsc.org/advances

ZnO nanoparticles-functionalized WO_3 plates with enhanced photoelectrochemical properties

Yang Liu[1]†, Haizhou He[1]†, Jie Li[1], Wenzhang Li[1,*], Yahui Yang[2], Yaomin Li [3], Qiyuan Chen[1]

[1]*School of Chemistry and Chemical Engineering, Central South University, Changsha 410083, China*

[2]*College of Resources and Environment, Hunan Agricultural University, Changsha 410128, China*

3 Department of Chemistry，University College London，20 Gordon Street，London，WC1H 0AJ，UK

[*]Corresponding author. Tel.: +86 731 8887 9616; fax: +86 731 8887 9616.

E-mail addresses: liwenzhang@csu.edu.cn,

† Contributed equally to this work

Table of contents entry

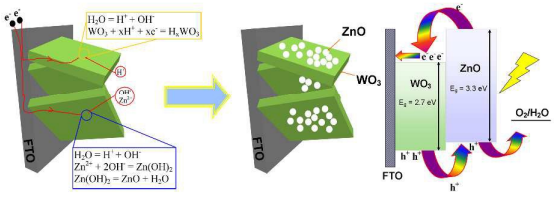

ZnO nanoparticles-functionalized WO_3 plates were prepared via the electrodeposition and the electrochromism reaction of WO_3, and the composites improve the separation of photogenerated electrons and holes.

Abstract

In this work, ZnO NPs-functionalized WO_3 vertical plate-like arrays were first fabricated on FTO with a hydrothermal process for WO_3 vertical plate-like arrays and an electrodeposition process for the functionalization of ZnO. The ZnO nanoparticles are preferentially loaded on the active points of WO_3 in the shape of sphere about 10 nm. The samples were characterized by various techniques, including X-ray diffraction (XRD), scanning electron microscopy (SEM) and transmission electron microscopy (TEM). Photolectrochemical properties were investigated by photoelectrochemical measures, such as linear sweep voltammogram, electrochemical impedance spectroscopy (EIS), intensity-modulated photocurrent spectroscopy (IMPS) and incident photon to current conversion efficiency (IPCE). The results show that the photocurrent of WO_3 increases from 0.88 to 1.23 mA/cm^2 at 1.2 V (vs Ag/AgCl) after functionalized with ZnO. Furthermore, the lifetime of the electron-hole has been prolonged from 6.44 to 8.56 ms, but there is no decrease in the electron transport time. In this case, the enhancement of photoelectrochemical performance is attributed to effectively transfer photo-generated holes so as to retard the recombination of electrons and holes.

Key words: WO_3, ZnO, hole transferance, photoelectrochemical performance

Introduction

Since the discovery of photoelectrochemical (PEC) water splitting using n-type TiO_2, hydrogen production by water dissociation has attracted great interest.[1] As a cheap and nontoxic material, TiO_2 and modified TiO_2 have been used as photocatalysts.[2-5] However, the wide bandgap energy which only allows absorption of

UV light, restricts its efficiency in PEC devices. With the research progresses of photoelectrochemical water splitting and photocatalysis, various kinds of semiconductors are also invented and employed.[6-9] Among them, WO_3, which is widely used as photocatalysis and gases sensing, is a suitable semiconductor because of some promising characteristics such as a suitable band gap (2.5-2.8 eV) that can utilize a portion of the visible light and excellent stability to avoid photocorrosion.[10-14]

In order to further improve the photoelectrochemical performance of WO_3 to fulfill the need of photolysis of water, two strategies have been adopted. One is to change its particle size or morphology, such as mesoporous, flower, nanorod and nanotube-based bundles.[15-18] For the WO_3 loaded on the FTO or ITO, the films have been prepared as nanowires, nanorods and nanoflakes.[11, 19, 20] The other approach to improve the photoelectrochemical properties is metal or non-metal element doping,[21-23] noble metal depositon,[24-26] graphene modifying[27, 28] or semiconductor coupling.[29-32] Among these, semiconductor coupling is an effective method to promote the separation of the photo-generated electron-hole pairs because the valence and conduction band positions are different from each other. Therefore, the recombinations of electrons and holes are stymied, and the efficiency of water splitting is enhanced.

For the WO_3 based semiconductor material, numerous semiconductors ($BiVO_4$, $NiWO_4$, $ZnWO_4$ and C_3N_4) were used as a second semiconductor to form composites with WO_3.[29-32] All of these systems indicated that an appropriate amount of second semiconductor is best for the efficiency of photolysis of water. It is because that the

excessive second semiconductor might play the role of obstacles that impede the contact of the WO_3 surface and the electrolyte solution. The second semiconductor loaded on the active sites of the base semiconductor can accelerate the separation of photo-generated electron-hole. So the selective loading is a great approach to improve the photoelectrochemical performance of WO_3.

In this paper, we selectively loaded ZnO on the active sites of WO_3 plates preferentially via the electrodeposition and the electrochromism reaction of WO_3. Moreover, we have studied the photoelectrochemical performances by liner sweep voltammogram, electrochemical impedance spectroscopy (EIS), intensity-modulated photocurrent spectroscopy (IMPS) and incident photon to current conversion efficiency (IPCE). It was found that the visible-light-driven photoelectrochemical properties of ZnO nanoparticles-functionalized WO_3 were enhanced as compared to the pristine WO_3 plates, and the possible mechanism for the enhanced photoelectrochemical performances was discussed on the basis of the obtained experimental results.

2 EXPERIMENTAL SECTION

2.1 Preparation of WO_3/ZnO

WO_3 plates were prepared from Na_2WO_4 by hydrothermal methods that had been well documented in our previous work.[20] A three electrode system was used for electrodeposition. The as prepared WO_3 film was used as a working electrode (1×1.5 cm^2) while platinum sheet and Ag/AgCl (saturated KCl) were used as counter electrode and reference electrode, respectively. The electrodepositing process was

carried out at the potential of -0.7 V (vs. Ag/ AgCl) for 30 s from unstirred aqueous solution of 0.01 mol • L^{-1} $Zn(NO_3)_2$ and 0.1 mol • L^{-1} KCl. The electrolyte (bath) temperature was maintained at 55°C after purged with oxygen for 10 min. Then the product was annealed at 350 °C for 30 min under air. So the sample was fabricated and labelled as WO_3/ZnO. For comparison, WO_3 plates film (labelled as WO_3) was also prepared without electrodeposition.

2.2 Characterization

For the structural studies, X-ray diffraction (XRD) patterns were recorded using X-ray diffractometer (XRD, D/Max2250) in the diffraction angle (2θ) between 10 ° and 70 °. Scanning electron microscopy (SEM, JSM6700F) and transmission electron microscope (TEM, TECNAI G2 F20) were used to observe the morphologies and microstructures of the samples. UV-Vis diffused reflectance spectroscopy was carried out by an UV-Vis spectrometer (UV-Vis, Shimadzu 2450). XPS measurements were taken using a X-ray photoelectron spectrograph (XPS, ESCALAB 250Xi, ThermoFisher-VG Scientific). Photoelectrochemical test systems were composed of a standard three-electrode configuration. The WO_3 or WO_3/ZnO film with a Pt counter electrode and an Ag/AgCl reference electrode were immersed in a 0.2 mol • L^{-1} Na_2SO_4 solution. A 500 W Xe lamp served as the visible light source, and a 420 nm cutoff filter was placed on the path of the Xe lamp to remove UV irradiation.

3. Results and discussion

3.1 Preparation of Characterization the films

As shown in Fig. 1, the reaction mechanism can be summarized as:

$$Zn(NO_3)_2 = Zn^{2+} + 2NO_3^- \quad (1)$$

$$H_2O = H^+ + OH^- \quad (2)$$

$$Zn^{2+} + 2OH^- = Zn(OH)_2 \quad (3)$$

$$Zn(OH)_2 = ZnO + H_2O \quad (4)$$

$$WO_3 + xH^+ + xe^- = H_xWO_3 \quad (5)$$

Because the reaction equation (5) [33]preferentially occurred at the active sites of WO_3, near which the pH of the electrolyte shifts towards high value. Zn^{2+} in the interface region of semiconductor-electrolyte tended to form ZnO or $Zn(OH)_2$, which can be seen in the potential–pH diagram of T. Pauporté's work.[34] So ZnO or $Zn(OH)_2$ can be loaded on the active sites of WO_3. In order to improve the $Zn(OH)_2$ convert to ZnO and the contact between ZnO and WO_3, the samples were annealed, and ZnO NPs-functionalized WO_3 vertical plate-like arrays were fabricated on FTO.

The crystallographic properties of the as-prepared films were measured using XRD measurements. The corresponding results are shown in Fig. 2. It can be easily seen that the XRD data for the WO_3 and WO_3/ZnO film match well with the monocline WO_3 (PDF#72-0677) and tetragonal structure of SnO_2 (PDF#46-1088). There is no detection of ZnO phases in the patterns of XRD. It can be explained with two reasons. One is that the concentration of ZnO is too low to be detected by XRD. The other is that the zinc species in the sample are dispersing on the surface of WO_3 plates uniformly and sparsely.

The morphology and microstructure of the WO_3 and WO_3/ZnO were investigated by SEM and TEM. Fig. 3 gives representative top-views and cross-views of the

samples. In Fig. 3a and 3b, the low-magnification SEM images show that both samples present overall plate-like structure. The high-magnification SEM images in inset of Fig. 3a and 3b present almost the same morphology, while the thicknesses of plates are around 240-500 nm. And the cross sectional SEM images (Fig.3a and 3b) show the same thickness of film about 1.63 μm. In other words, the nanostructures are well retained after electrodeposition and annealing. More details of morphological and structural features were studied using TEM and shown in Fig. 4. The EDS of WO_3/ZnO shown in Fig.S1 reveals the presence of W, O and Zn, and the diffraction patterns shown in Fig.S2 are indexed to the monocline WO_3. The image in Fig. 4a displays the stagger plate-like structure of the as prepared WO_3/ZnO. It can be observed that a lot of nanoparticles attach the surface of plates. From the high-magnification TEM image in Fig. 4b, the lattice fringe of nanoparticle is about 0.260 nm which corresponds to the interplanar spacing of (200) plane of ZnO.

XPS was performed to know the surface chemical composition and the oxidation state of the as-prepared film. The XPS peaks indicate that the film contains W, O, Zn and C. The signal of C originates from the adventitious hydrocarbon in the XPS instrument itself. Fig. 5 shows the high-resolution XPS spectra of W 4f, O 1s, and Zn 2p, respectively. Two peaks at 35.56 and 37.71 eV in the spectrum were assigned to W $4f_{7/2}$ and W $4f_{5/2}$, respectively, which are consistent with the reported values.[33] The asymmetric O1s peak was fitted by three peaks, centered at 530.2 eV (O-Zn), 530.5 eV (O-W) and 532.6 (surface hydroxyl).[35] The binding energies of Zn $2p_{1/2}$ and Zn $2p_{3/2}$ are respectively located at 1044.05 and 1021.05 eV, with a spin energy

separation of 23 eV.[36] The above results indicate that ZnO nanoparticles are successfully decorated on WO_3 plates, and the molar content of loaded ZnO is determined by XPS to be 2.02 mol. %.

Fig. S3 shows the UV-Vis absorption spectra of WO_3 and WO_3/ZnO. The UV-Vis spectrum of the WO_3 indicates that it absorbs light with a wavelength less than 465 nm, corresponding to 2.67 eV of band gap energy. There is a slight blue-shift in the absorption edge of WO_3/ZnO, which is 460 nm corresponding to 2.70 eV of band gap energy. At the wavelengths >465 nm, the absorbance of both samples are almost the same. So we believe that the light absorption ability has not been improved in this system.

3.2 Photoelectrochemical measurements of the films

Fig. 6a shows the transient photocurrent responses with several on-off cycles of intermittent light irradiation (>420 nm) at 1.0 V (vs. Ag/AgCl). As can be seen, the photocurrent value rapidly decreases to about zero as soon as the light turns off, and the photocurrent comes back to a constant value when the light is on again. These results are well reproducible. Within the first few seconds of illumination, a slight photocurrent decay was obsrved for each sample. It may have two reasons. One is that concentrated gradient exists at the interface of photoanode and electrolyte, which is because the photoelectrochemical properties were measured in the 0.2 $mol \cdot L^{-1}$ Na_2SO_4 solution without stirring. The other, which is more important, is that sudden irradiation leads to rapid initial generation of electron-hole pairs and a great photocurrent excitement at the early stage of the illumination. From the beginning of irradation to the end of measure, the photocurrent of WO_3 decreases 33.3% (from 1.01

to 0.67 mA/cm^2). The WO_3/ZnO exhibits higher photocurrent than that of the bare WO_3 under visible irradiation, and the photocurrent decreases 22.2% (from 1.22 to 0.95 mA/cm^2). It means that the composite structure film shows better stability compared to the bare WO_3.

Fig. 6b shows the liner sweep voltammogram measurements under visible light irradiation for the WO_3 and WO_3/ZnO electrodes at a scan rate of 20 mV/s. The photocurrent values of both electrodes increase with the upgrade of applied potential of the working electrode. The photocurrent densities of the WO_3 and WO_3/ZnO at 1.2 V (vs Ag/AgCl) are about 0.88 and 1.23 mA/cm^2, respectively. The photoelectrochemical properties of photoanodes fabricated with WO_3 and WO_3/ZnO plates are also evaluated by the light energy to chemical energy efficiency, which is calculated as an equation.[37, 38]

$$\varepsilon(\%) = j_p \{(E_r^0 - |E_a|)\} / I_o \times 100$$

In this equation, j_p, E_r^0, E_a and I_o are the photocurrent density, the standard reversible potential, applied potential of the working electrode and power density of the incident light, respectively. As shown in Fig. 6c, the maximum photoconversion efficiency of WO_3/ZnO (0.475%) is greater than that of WO_3 (0.339%).

Following liner sweep voltammogram measurements, EIS measurements were used to investigate the properties of electron transfer resistance across the semiconductor-electrolyte interfaces under visible irradiation. It is well known that EIS Nyquist plots can be used to characterize the charge transfer resistance and the separation efficiency of the photo-generated electrons and holes. Fig. 7a shows the

Nyquist plots of samples at an AC frequency varying from 10 kHz to 0.1 Hz under the bias of 0.7 V (vs Ag/AgCl). Each of the electrodes presents a semicircle, which can be fitted to an equivalent circuit including a series resistance (R_s), a charge transfer resistance (R_{ct}) and a constant phase element (*CPE*), and the equivalent circuit is exhibited in the inset of Fig. 7a. Bode-phase plots of the EIS spectra for the samples are shown in Fig. 7b. The maximum oscillation frequency (f_{max}) of the impedance semicircle of WO_3/ZnO is less than that of WO_3. Thus, the corresponding lifetime of photoelectrons in WO_3/ZnO increases according to the formula ($\tau = 1/2\pi f_{max}$).[39] And the values of τ are 6.44 and 8.56 ms for WO_3 and WO_3/ZnO, respectively. It can be ascribed to efficient separation of the light-generated electrons and holes in the WO_3/ZnO. In other words, the electrons transfer from the conduction band of WO_3 to the FTO, while the holes are transported to the valence band of the ZnO. So the recombination of electron-hole pairs are inhibited, and lifetime of photoelectrons are prolonged.

Mott−Schottky is used to determine the flat band potential of each semiconductor material. As shown in the Fig. S4, the flat band potentials for WO_3 and WO_3/ZnO are -0.168 and -0.198 V (vs Ag/AgCl), respectively, which are calculated from the x-intercept of the linear portion of the Mott−Schottky plots. It means that the shift in the Fermi level to negative potential is about 0.03 V after modified with ZnO.[40]

In order to identify the main factor of the enhancement of photoelectrochemical properties, intensity-modulated photocurrent spectroscopy (IMPS) was carried out to

investigate electron transport. The lamp-house was fitted with a blue light emitting diode (LED) (390 nm) driven by a PP210 (Zahner) frequency response analyser. Fig. 8 shows the complex plane spectra of the IMPS response. The electron transport time (τ_n) can be determined from the frequency at the imaginary maximum (f_{im}), given by the formula ($\tau_n = 1/2\pi f_{im}$).[29] The electron transport time calculated for WO_3 and WO_3/ZnO is 2.35 and 2.97 ms, respectively. The slightly longer electron transport time might be caused by the electron transfer from the conduction band of ZnO to FTO via the conduction band of WO_3. However, the content of ZnO is too little to generate much electrons. Considering the light source for other photoelectrochemical measurements is filtered by a 420 nm cutoff filter, the photo-generated electrons produced by ZnO are negligible. The above results confirm that the photo-generated holes of WO_3 transferred to the valence band of ZnO improve the separation of electrons and holes so as to enhance the photoelectrochemical performance of the electrode.

The photocurrent responses of samples as a function of wavelength of incident light were measured at a bias of 1.2 V. The calculated incident photon to current conversion efficiency (IPCE) is shown in Fig. 9. The IPCE of WO_3 drops to zero at wavelengths longer than 470 nm, which is consistent with the results of UV-Vis spectra. In the photoresponse region, WO_3/ZnO shows a better IPCE value than WO_3. Both photoanodes display a maximum IPCE value at the wavelength of around 360 nm. In the case of the WO_3/ZnO film, the maximum IPCE value is 47.24%, whereas WO_3 is 28.88%. Because of the similar photoresponse region of WO_3 and WO_3/ZnO,

the enhancement of IPCE indicates that the effective inhibition in the recombination of electron-hole pairs by transferring the photo-generated holes is a great choice for improving the photoelectrochemical properites.

A simple mechanism of the conduction and valence band positions for a WO_3/ZnO composite structure is shown in Fig. 10. As can be seen, ZnO has neglectful activity under visiable light, and much less photoactive than WO_3. However, when formed into a composite with WO_3, electrons excited into the conduction band of ZnO can transfer to the current collector via the conduction band of the WO_3. More importantly, the valence band edge of the ZnO is at a higher energy than the valence band edge of the WO_3. The holes leaving in the valence band of WO_3 can move into the valence of ZnO, which facilate the electron/hole separation. Therefore, it can be concluded that the WO_3/ZnO has a better photoelectrochemical performance than WO_3 by promoting electron/hole separation.

Conclusion

In summary, ZnO NPs-functionalized WO_3 vertical plate-like arrays film was first synthesized by a combination of hydrothermal and electrodeposition methods, and characterized by various techniques. Experimental results indicate that ZnO NPs-functionalized WO_3 has a higher photocurrent under visible light irradiation. And the photoconversion efficiency is greater than that of bare WO_3. On the basis of EIS, IMPS and IPCE, the high photoelectrochemical performance can be attributed to the effective transfer of the photo-generated holes retarding the recombination of electrons and holes. The combination of electrodeposition and the electrochromism

reaction of WO_3 provide an approach to synthesize WO_3 based 1D or 2D composite materials film.

Acknowledgements

This study was supported by the National Nature Science Foundation of China (No. 21171175), the Hunan Provincial Natural Science Foundation of China (No. 13JJ6003), the Open-End Fund for the Valuable and Precision Instruments of Central South University.

References

1. A. Fujishima and K. Honda, *Nature*, 1972, 238, 37-38.
2. W. Zhou, W. Li, J.-Q. Wang, Y. Qu, Y. Yang, Y. Xie, K. Zhang, L. Wang, H. Fu and D. Zhao, *Journal of the American Chemical Society*, 2014, 136, 9280-9283.
3. G. Wang, H. Wang, Y. Ling, Y. Tang, X. Yang, R. C. Fitzmorris, C. Wang, J. Z. Zhang and Y. Li, *Nano Letters*, 2011, 11, 3026-3033.
4. S. Hoang, S. P. Berglund, N. T. Hahn, A. J. Bard and C. B. Mullins, *Journal of the American Chemical Society*, 2012, 134, 3659-3662.
5. K. Li, B. Chai, T. Peng, J. Mao and L. Zan, *ACS Catalysis*, 2013, 3, 170-177.
6. X. Guan and L. Guo, *ACS Catalysis*, 2014, 4, 3020-3026.
7. K. Chang, Z. Mei, T. Wang, Q. Kang, S. Ouyang and J. Ye, *ACS Nano*, 2014, 8, 7078-7087.
8. L. Zhang, D. Jing, L. Guo and X. Yao, *ACS Sustainable Chemistry & Engineering*, 2014, 2, 1446-1452.
9. P. Zhou, J. Yu and M. Jaroniec, *Advanced Materials*, 2014, 26, 4920-4935.
10. P. M. Rao, L. Cai, C. Liu, I. S. Cho, C. H. Lee, J. M. Weisse, P. Yang and X. Zheng, *Nano Letters*, 2014, 14, 1099-1105.
11. J. Y. Zheng, G. Song, C. W. Kim and Y. S. Kang, *Nanoscale*, 2013, 5, 5279-5282.
12. L. Yin, D. Chen, M. Hu, H. Shi, D. Yang, B. Fan, G. Shao, R. Zhang and G. Shao, *Journal of Materials Chemistry A*, 2014, 2, 18867-18874.
13. L. Yin, D. Chen, M. Feng, L. Ge, D. Yang, Z. Song, B. Fan, R. Zhang and G. Shao, *RSC Advances*, 2015, 5, 328-337.
14. D. Chen, L. Yin, L. Ge, B. Fan, R. Zhang, J. Sun and G. Shao, *Sensors and Actuators B: Chemical*, 2013, 185, 445-455.
15. O. Yayapao, T. Thongtem, A. Phuruangrat and S. Thongtem, *Journal of Alloys and Compounds*, 2011, 509, 2294-2299.
16. R. Solarska, B. D. Alexander, A. Braun, R. Jurczakowski, G. Fortunato, M. Stiefel, T. Graule and J. Augustynski, *Electrochimica Acta*, 2010, 55, 7780-7787.
17. V. B. Patil, P. V. Adhyapak, S. S. Suryavanshi and I. S. Mulla, *Journal of Alloys and Compounds*, 2014, 590, 283-288.
18. P. M. Rao, I. S. Cho and X. Zheng, *Proceedings of the Combustion Institute*, 2013, 34, 2187-2195.
19. J. Su, X. Feng, J. D. Sloppy, L. Guo and C. A. Grimes, *Nano Letters*, 2010, 11, 203-208.
20. J. Yang, W. Li, J. Li, D. Sun and Q. Chen, *Journal of Materials Chemistry*, 2012, 22, 17744-17752.
21. Y. Sun, C. J. Murphy, K. R. Reyes-Gil, E. A. Reyes-Garcia, J. M. Thornton, N. A. Morris and D. Raftery, *International Journal of Hydrogen Energy*, 2009, 34, 8476-8484.
22. W. Mu, X. Xie, X. Li, R. Zhang, Q. Yu, K. Lv, H. Wei and Y. Jian, *RSC Advances*, 2014, 4, 36064-36070.
23. M.-T. Chang, L.-J. Chou, Y.-L. Chueh, Y.-C. Lee, C.-H. Hsieh, C.-D. Chen, Y.-W. Lan and L.-J. Chen, *Small*, 2007, 3, 658-664.
24. S. Sun, W. Wang, S. Zeng, M. Shang and L. Zhang, *Journal of Hazardous Materials*, 2010, 178, 427-433.

25. A. Tanaka, K. Hashimoto and H. Kominami, *Journal of the American Chemical Society*, 2013, 136, 586-589.
26. D. Chen, T. Li, Q. Chen, J. Gao, B. Fan, J. Li, X. Li, R. Zhang, J. Sun and L. Gao, *Nanoscale*, 2012, 4, 5431-5439.
27. X. Chang, L. Dong, Y. Yin and S. Sun, *RSC Advances*, 2013, 3, 15005-15013.
28. Y. Liu, W. Li, J. Li, Y. Yang and Q. Chen, *RSC Advances*, 2014, 4, 3219-3225.
29. J. Su, L. Guo, N. Bao and C. A. Grimes, *Nano Letters*, 2011, 11, 1928-1933.
30. K. C. Leonard, K. M. Nam, H. C. Lee, S. H. Kang, H. S. Park and A. J. Bard, *The Journal of Physical Chemistry C*, 2013, 117, 15901-15910.
31. J. Zhu, W. Li, J. Li, Y. Li, H. Hu and Y. Yang, *Electrochimica Acta*, 2013, 112, 191-198.
32. Y. Zang, L. Li, Y. Zuo, H. Lin, G. Li and X. Guan, *RSC Advances*, 2013, 3, 13646-13650.
33. S. Cong, Y. Tian, Q. Li, Z. Zhao and F. Geng, *Advanced Materials*, 2014, 26, 4260-4267.
34. A. Goux, T. Pauporté, J. Chivot and D. Lincot, *Electrochimica Acta*, 2005, 50, 2239-2248.
35. P. T. Hsieh, Y. C. Chen, K. S. Kao and C. M. Wang, *Appl Phys A*, 2008, 90, 317-321.
36. M. Shao, F. Ning, M. Wei, D. G. Evans and X. Duan, *Advanced Functional Materials*, 2013, 24, 580-586.
37. P.-T. Hsiao, L.-C. Chen, T.-L. Li and H. Teng, *Journal of Materials Chemistry*, 2011, 21, 19402-19409.
38. A. Devadoss, P. Sudhagar, C. Ravidhas, R. Hishinuma, C. Terashima, K. Nakata, T. Kondo, I. Shitanda, M. Yuasa and A. Fujishima, *Physical Chemistry Chemical Physics*, 2014, 16, 21237-21242.
39. K. Chen, X. Feng, R. Hu, Y. Li, K. Xie, Y. Li and H. Gu, *Journal of Alloys and Compounds*, 2013, 554, 72-79.
40. J. Zhang, J. H. Bang, C. Tang and P. V. Kamat, *ACS Nano*, 2009, 4, 387-395.

Figures

Fig. 1 Synthesis schematic of the ZnO NPs-functionalized WO_3 vertical plate-like arrays

Fig. 2 XRD patterns of the WO_3 and WO_3/ZnO films

Fig. 3 SEM images of the surface morphology of (a) WO_3 and (b) WO_3/ZnO; cross-sectional micrographs of (c) WO_3 and (d) WO_3/ZnO; high-magnification SEM images in inset of (a) and (b).

Fig. 4 Transmission electron micrographs and High resolution TEM (HRTEM) image of WO_3/ZnO

Fig. 5 XPS of WO_3/ZnO (a) full spectrum; (b) W 4f; (c) O 1s and (d) Zn 2p.

Fig. 6 (a) Photocurrent–time plots with chopping light at 1.0 V (vs. Ag/AgCl), (b) Linear sweep voltammograms and (c) Photoconversion efficiency of the as-prepared samples.

Fig. 7 EIS plots of the WO_3 and WO_3/ZnO: (a) Nyquist plots and (b) Bode plots.

Fig. 8 intensity-modulated photocurrent spectroscopies of WO_3 and WO_3/ZnO

Fig. 9 Incident photo to current conversion efficiency of WO_3 and WO_3/ZnO

Fig. 10 Schematic of conduction and valence band positions for transference of electrons and holes

Fig. S1 EDS of WO_3/ZnO

Fig. S2 SAED pattern of the WO_3/ZnO

Fig. S3 UV-Vis absorbance spectroscopy of the WO_3 and WO_3/ZnO

Fig. S4 Mott−Schottky plots of the WO_3 and WO_3/ZnO

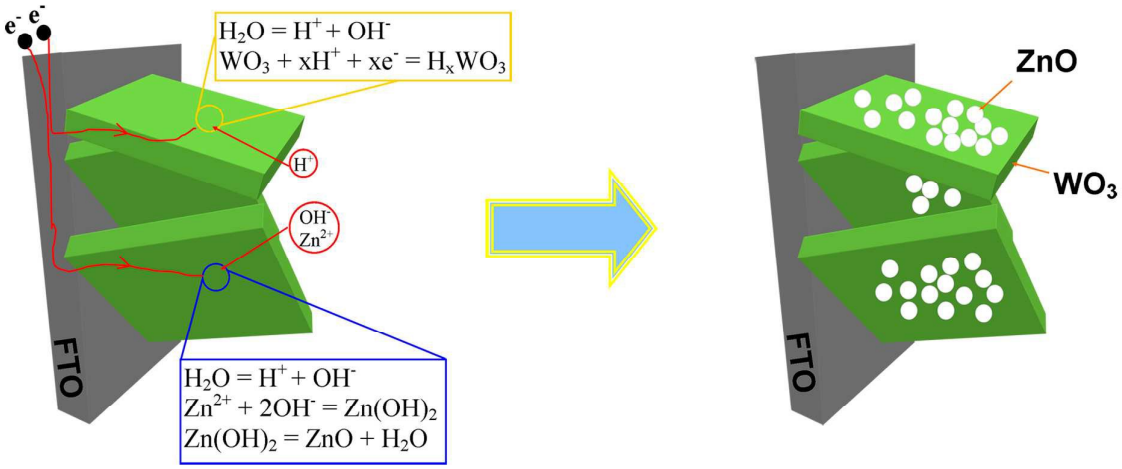

Fig. 1 Synthesis schematic of the ZnO NPs-functionalized WO_3 vertical plate-like arrays

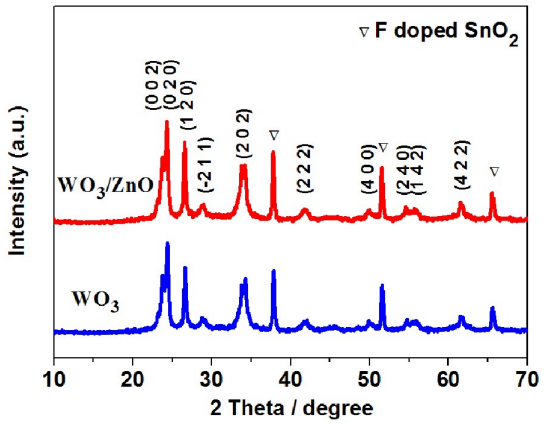

Fig. 2 XRD patterns of the WO_3 and WO_3/ZnO films

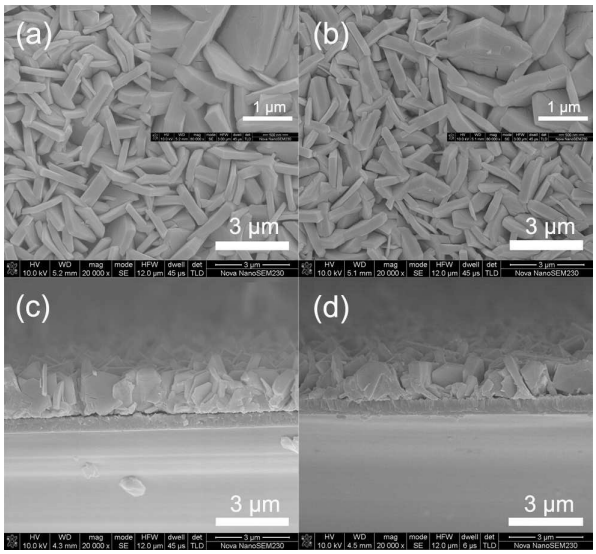

Fig. 3 SEM images of the surface morphology of (a) WO_3 and (b) WO_3/ZnO; cross-sectional micrographs of (c) WO_3 and (d) WO_3/ZnO; high-magnification SEM images in inset of (a) and (b).

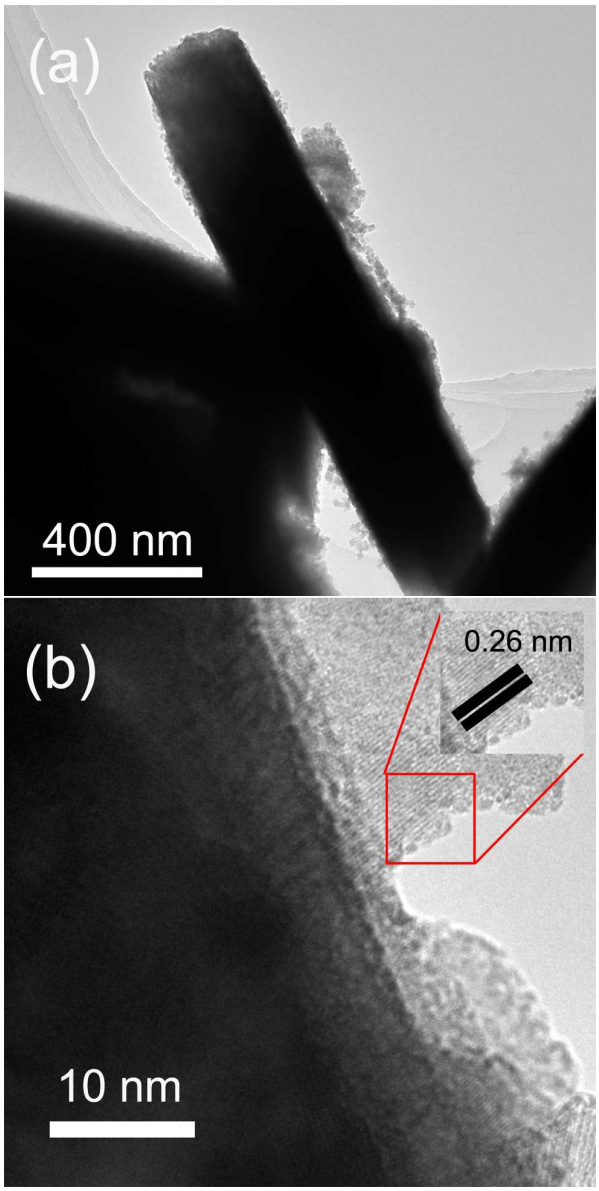

Fig. 4 Transmission electron micrographs and High resolution TEM (HRTEM) image of WO_3/ZnO

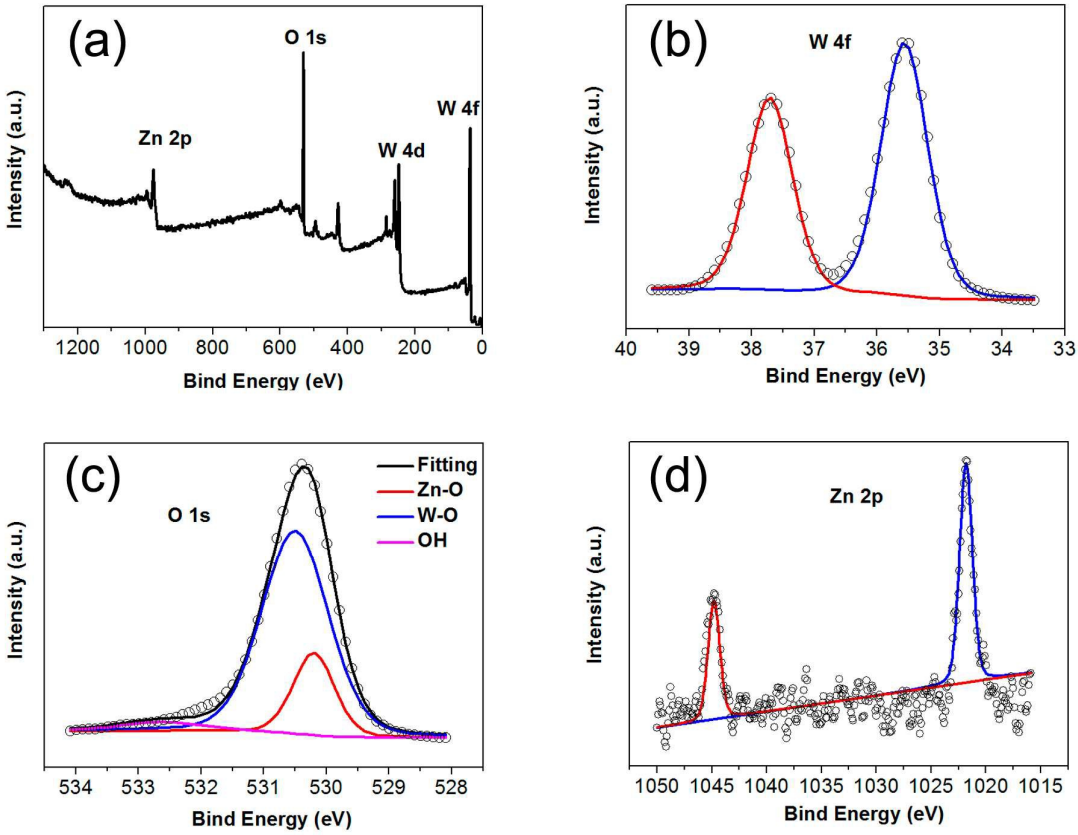

Fig. 5 XPS of WO_3/ZnO (a) full spectrum; (b) W 4f; (c) O 1s and (d) Zn 2p.

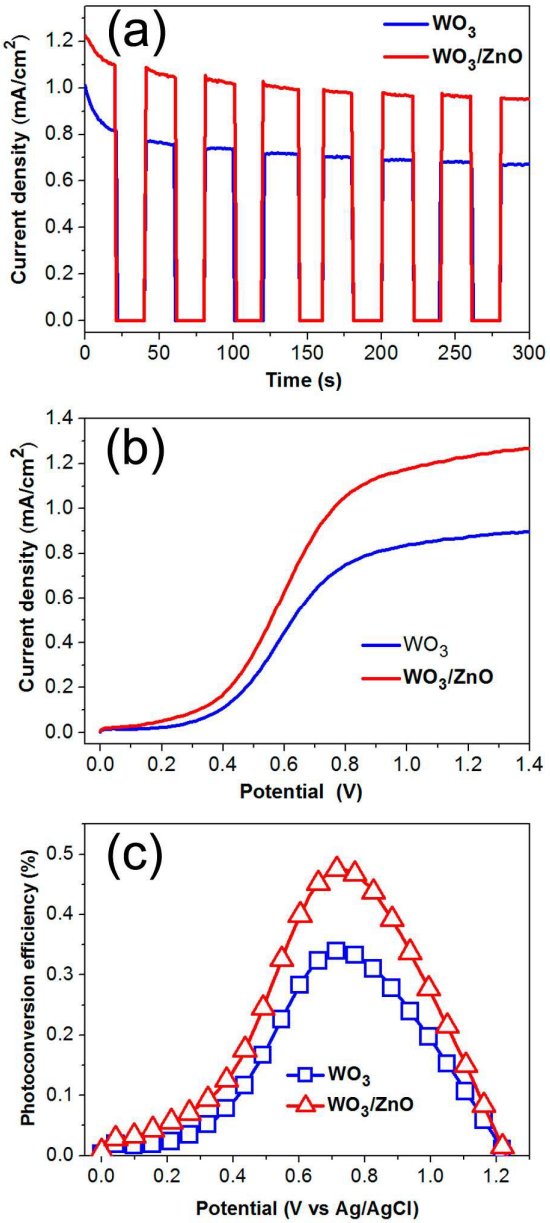

Fig. 6 (a) Photocurrent–time plots with chopping light at 1.0 V (vs. Ag/AgCl), (b) linear sweep voltammograms and (c) photoconversion efficiency of the as-prepared samples.

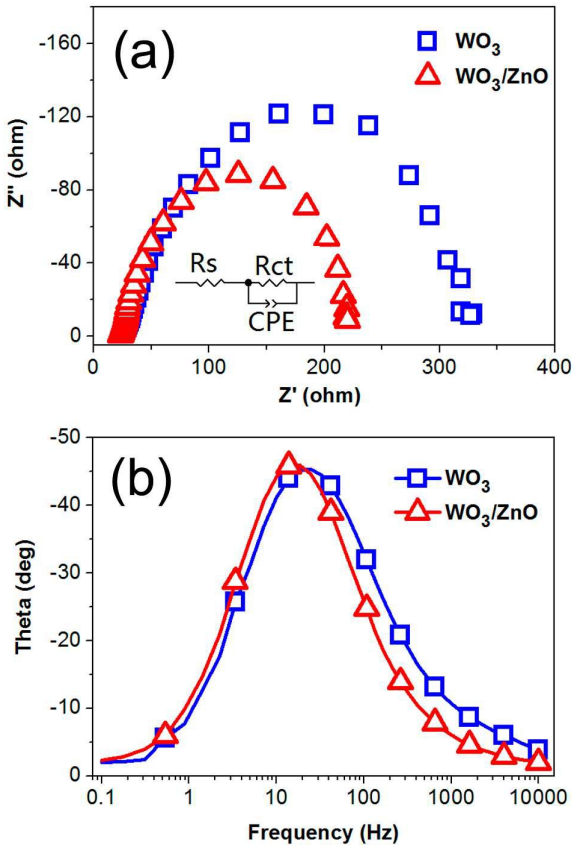

Fig. 7 EIS plots of the WO_3 and WO_3/ZnO: (a) Nyquist plots and (b) Bode plots.

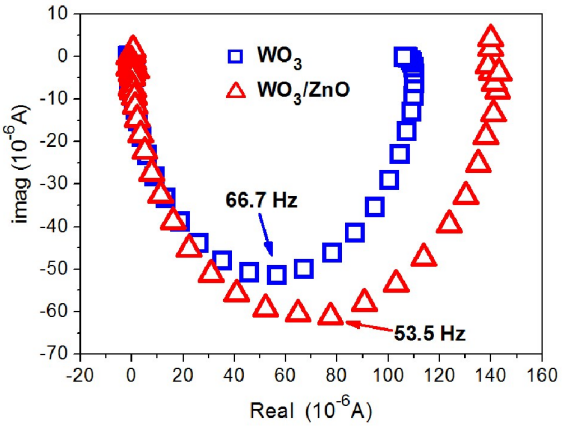

Fig. 8 Intensity-modulated photocurrent spectroscopies of WO_3 and WO_3/ZnO

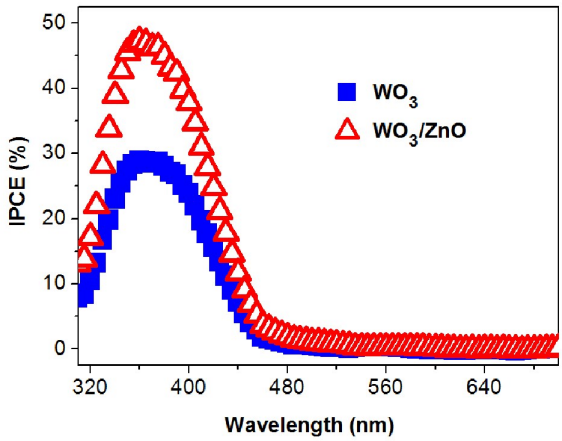

Fig. 9 Incident photo to current conversion efficiency of WO_3 and WO_3/ZnO

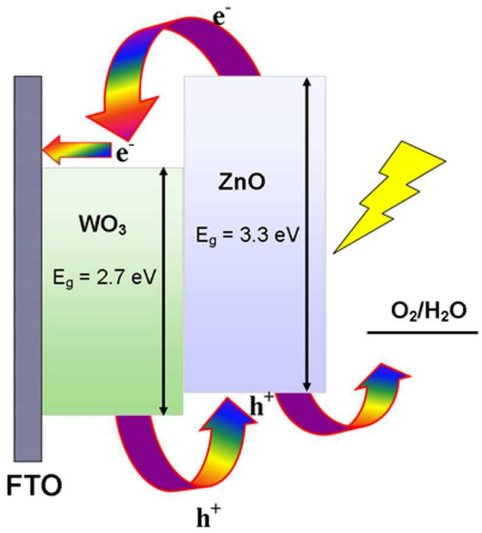

Fig. 10 Schematic of conduction and valence band positions for transference of electrons and holes